

Effects of radial aerodynamic forces on rotor-bearing dynamics of high-speed turbochargers

A Alsaeed¹, G Kirk² and S Bashmal¹

Proc IMechE Part C:
J Mechanical Engineering Science
 0(0) 1–17
 © IMechE 2014
 Reprints and permissions:
sagepub.co.uk/journalsPermissions.nav
 DOI: 10.1177/0954406214520817
pic.sagepub.com


Abstract

This study investigates the radial aerodynamic forces that may develop inside the centrifugal compressor and the turbine volutes due to pressure variation of the circulating gas. The forces are numerically predicted for magnitudes, directions, and locations. The radial aerodynamic forces are numerically simulated as static forces in the turbocharger finite element model with floating ring bearings and solved for nonlinear time-transient response. The numerical predictions of the radial aerodynamic forces are computed with correlation to earlier experimental results of the same turbocharger. The outcomes of the investigation demonstrate a significant influence of the radial aerodynamic loads on the turbocharger dynamic stability and the bearing reaction forces. The numerical predictions are also compared with experimental results for validation.

Keywords

Vibration, turbocharger, stability, aerodynamic, bearings, compressor, turbines

Date received: 10 June 2013; accepted: 28 November 2013

Introduction

Automotive turbochargers are turbomachines intended to increase the power of internal combustion engines by compressing excess air into the engine cylinder. Turbocharging has become standard for most diesel engines and is used in many gasoline engines as well.¹ For the past few decades, engineers and researchers have attempted to improve turbocharger designs for better performance and lower manufacturing cost. A common design assembly consists of a radial outflow compressor and a radial inflow turbine on a single shaft. Bearings are mounted inboard, with the compressor and turbine overhung.

The primary consideration in the rotor-dynamic design of high-speed machinery is to control and minimize vibration. Large-amplitude vibration is undesirable as it generates noise and can have large amplitudes that cause rotor–stator rub.² Self-excited vibrations usually occur at frequencies that are a fraction, rather than a multiple, of shaft speed. Such sub-synchronous vibrations (below rotor shaft operating frequency) do not require a driving imbalance in the rotating element but are due to the interaction between the inertia and elasticity of the rotating elements and the aerodynamic forces on the rotor and hydrodynamic forces in the bearings. These instabilities usually increase in amplitude as the running

speed increases, until nonlinearities in the system forbid higher amplitudes or failure occurs.

San Andres and Kerth³ presented a thermal flow analysis coupled with a nonlinear rotor dynamic analysis for prediction of the steady-state and transient response of an automotive turbocharger supported on floating ring journal bearings. The nonlinear transient results predict the frequency content of the measured response with fair accuracy, but the model usually overpredicts the amplitude of rotor response. Poor knowledge of the actual rotor imbalance distribution could explain the discrepancies. Predicted ring speed ratios decrease as the shaft speed increases, mainly owing to thermal effects on the operating clearances and film viscosities. However, the test results show more dramatic reductions in ring speeds. Aerodynamic loads arising from an uneven pressure distribution in the compressor volute when operating away from its best efficiency point appear to affect the

¹Department of Mechanical Engineering, King Fahd University of Petroleum and Minerals, Saudi Arabia

²Department of Mechanical Engineering, Virginia Polytechnic Institute and State University, USA

Corresponding author:

S Bashmal, Department of Mechanical Engineering, King Fahd University of Petroleum and Minerals, PO Box 399, Building 22, Room 207, Dhahran 31261, Saudi Arabia.
 Email: bashmal@kfupm.edu.sa

turbocharger dynamic performance. The study recommends that tests with the compressor housing oriented at various angles may reveal the noted influence.

Many recent studies have pointed out the significance of aerodynamic forces and their effect on the turbocharger performance. The volute radial aerodynamic forces on either the compressor or turbine wheels in high-speed turbochargers have not been widely studied before. One of the few studies is the work of Flaxington and Swain,⁴ who attempted to describe how turbine vanes are designed in a way to minimize the thrust loads. They concluded that it is difficult to calculate an accurate thrust load value on the turbine wheel.⁴

Nowadays, the availability of powerful computers has enabled the simulation of flow and heat transfer in structures with complex geometries and multiphase fluid properties. A computational fluid dynamics (CFD) numerical model has been developed by Yao et al.⁵ to predict the flow behavior in the proximity of the nozzle vanes inside a turbocharger. The focus was to understand the flow distortion and aerodynamic loss and their effect on engine efficiency. The primary aim was to investigate the causes of aerodynamic loss, which was believed to be due to the interaction in the vanes of the guide and the nozzle. The effect of the aerodynamic forces on the stability and bearing forces is not considered.

Chen⁶ discussed the design aspects that affect the aerodynamic performance of turbochargers for applications in gasoline engines. He emphasized on the importance of improving the mechanical design of the compressor in order to achieve the best aerodynamic performance. The study by Chen⁶ also illustrated that unsteady flow in the volute housing of the compressor produces aerodynamic forces that have significant effect on bearing life and overall stability.

More recently, Romagnoli and his colleagues⁷⁻⁹ carried out experimental and numerical studies to evaluate the aerodynamic and thermal performance of turbocharger turbines under unsteady flow conditions. A meanline model was developed to predict the aerodynamic loss due different load and flow conditions.

While the cited studies contributed to the understanding of the aerodynamic performance in the turbocharger, their effect on the dynamic stability and bearing forces needs further investigation. The radial aerodynamic forces that may develop inside the centrifugal compressor and turbine volutes are studied in this article. The dynamic analysis of the turbocharger without radial aerodynamic loads is presented. The numerical predictions of the radial aerodynamic loads and their effects on the turbocharger dynamic stability and on bearing reaction forces and dynamics are followed. The current investigation begins with prediction of the radial aerodynamic forces developed inside the compressor and turbine volutes under normal operational conditions. The numerical

predictions of the radial aerodynamic forces are related to a former experimental study of a similar turbocharger in the Virginia Tech Rotor Dynamics Laboratory. The nonlinear time-transient analysis of the turbocharger with simulated static forces may help in the predictions of the locations, magnitudes, and directions of the radial aerodynamic loads that may develop inside the turbocharger casing. The effects on the dynamic stability as well as the bearing reaction forces are studied.

Experimental investigations of radial aerodynamic loads

Some recent experimental studies on the high-speed turbocharger dynamic stability^{3,10} discovered that there may be a considerable influence of the aerodynamic loads in the compressor and/or turbine volutes on the rotor. Eynon and Whitfield¹¹ studied the pressure recovery in a turbocharger compressor volute. At high flow rates, the gas accelerates around the volute and as a consequence the pressure decreases, whereas at flow rates less than that at design, the gas decelerates and a pressure rise occurs. The study illustrated that the volute provides a significant pressure rise at the best efficiency point and at flow rates down to full surge. In addition, it was shown that the volute performance is a function of inlet flow angle and that it plays a significant role in setting both the best efficiency flow rate and the operating range of the compressor.

Figure 1 shows the turbocharger test stand for a 3.9l 130 HP diesel engine with stock turbocharger that was built in the Virginia Tech Rotor Dynamics Laboratory in order to investigate the dynamic stability of the rotor-bearing system.¹⁰ The experimental results were successful in providing insight into this particular turbocharger's dynamic performance, which is believed to be typical of high-speed turbochargers operating on floating ring bearings. Reported measurements showed a side load force when the engine is loaded at full speed, which moves the shaft eccentric. Figure 2 represents the shaft centerline for the two test runs: the unloaded and loaded engine. For the no-load case, the shaft is centered for almost all of the run and then goes up on an arc as the speed drops below about 15,000 r/min, actual speed. The loaded case has more offsets as the engine is loaded and then at 30,000 r/min it re-centers and then follows the same arc to the upper portion of the bearing.

The radial aerodynamic force developed in either the compressor or the turbine volute is possibly due to pressure variation. That is, for high flow rates in the compressor for example, the gas accelerates around the volute and as a consequence the pressure decreases, whereas at flow rates less than that at design, the gas decelerates and a pressure rise occurs. The pressure variation is also dependent on several complicated factors, which can be divided

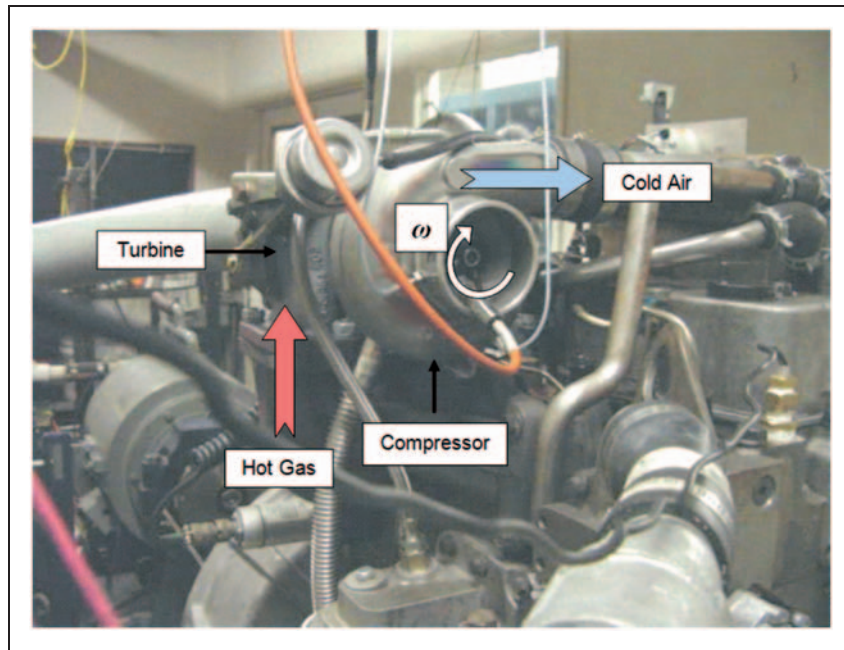
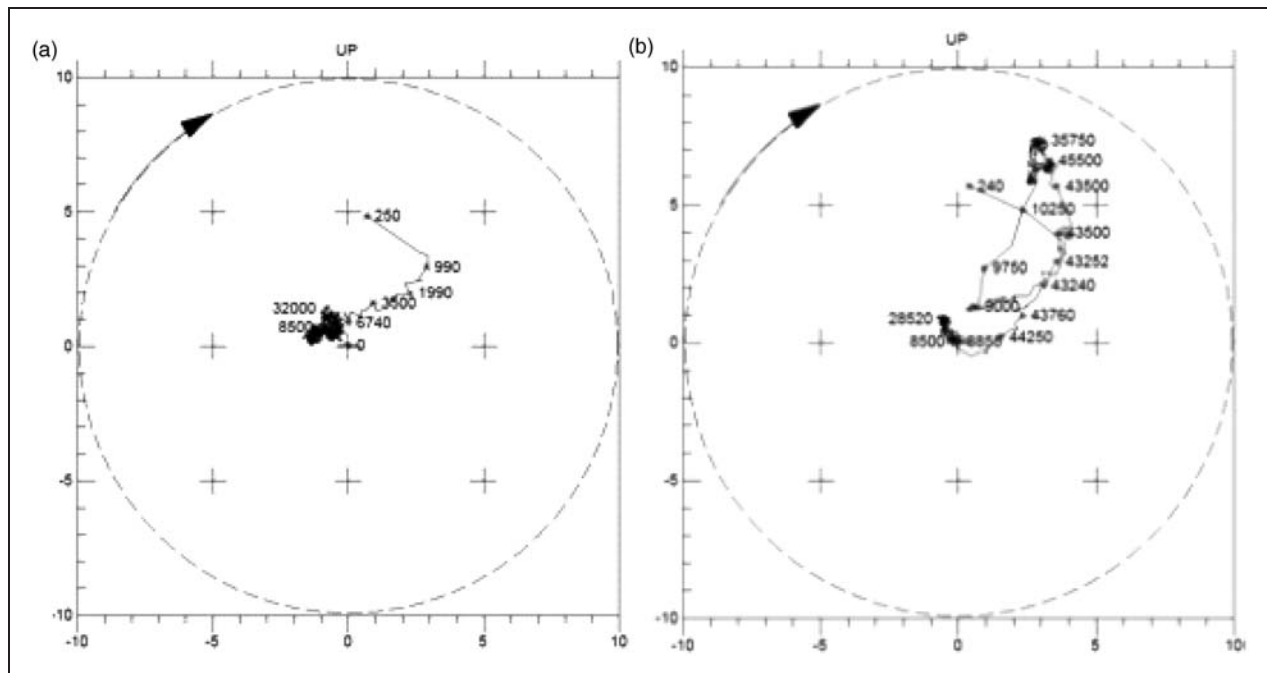


Figure 1. Turbocharger test stand. Compressor inlet showing optical speed sensor and dual probes. Dynamometer can be seen in lower left.



5 Figure 2. Centerline plot of compressor end shaft at target nut for: (a) no load and (b) full load. Keyphasor[®] at one-third; hence speeds shown are one-third of actual shaft speed in revolutions per minute.¹⁰

into static and dynamic components. The current study used both the theoretical and numerical analysis in the predictions of those radial forces.

Dynamic analysis of the unloaded turbocharger

The nonlinear analysis of the turbocharger rotor model, shown in Figure 3, with floating ring bearings

is used to predict the system transient response.¹² The finite element model (FEM) has been successfully used to perform steady-state, stability, and nonlinear transient analyses of the turbocharger dynamic response.^{13–15} Standard rotor dynamic considerations have been included for the current analysis. Distributed mass beam element is used for rotor shaft, rigid disks for the turbine disk and compressor impeller, bearing calculations by either stand-alone

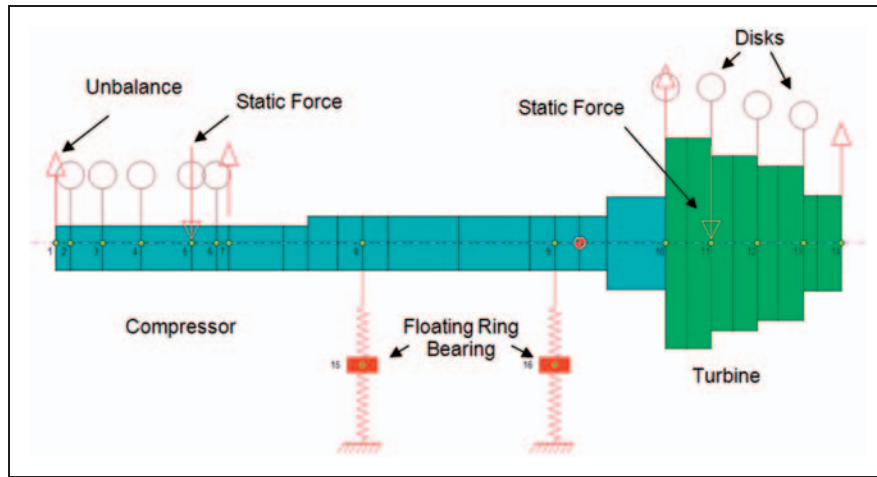


Figure 3. Turbocharger finite element model with simulated volute radial aerodynamic forces.

1 programs or built-in computer analysis. The floating ring bearings were described by eight linearized damping and stiffness parameters that can be obtained by solving the complete two-dimensional Reynolds equation. This is an iterative process that continues until the convergence criterion is satisfied. Once the static equilibrium is found, the eight bearing dynamic coefficients (stiffness and damping) are obtained by solving the perturbed pressure equations.¹² The steady-state position of the rotor shaft centerline is computed at speeds of 10, 20, 30, 40, 50, 60, 100, and 150 krpm. The objective is to trace the rotor shaft centerline and compare it with the above-mentioned experimental results.

Figure 4 shows the predicted rotor shaft centerline at the compressor end tip (station 1) with no-load conditions at speeds 10, 20, 30, 40, 50, 60, 100, and 150 krpm. Knowing that the horizontal axis of the experimental results shown in Figure 2 is opposite in direction to the analytical results shown in Figure 4, one may notice that both results show the shaft centerline having almost a straight line in the second quadrant (analytical coordinate system). The centerline angle is almost 45° from horizontal axis with x - y coordinates of (0.07, 0.07 mm), approximately at low speed of 10 krpm. Both results, analytical and experimental, agree on the fact that as rotor speed increased, the shaft centerline moves toward the origin point (0,0).

Analytical study of radial aerodynamic loads

Noncircular volute casing theory

The classical book on centrifugal flow pumps by Stepanoff¹⁶ discussed the volute radial aerodynamic forces. It was stated that most volute designs are non-circular in shape in order to reduce the radial thrust on the impeller as the rotor speed reaches the design speed. In the following, the same theory is

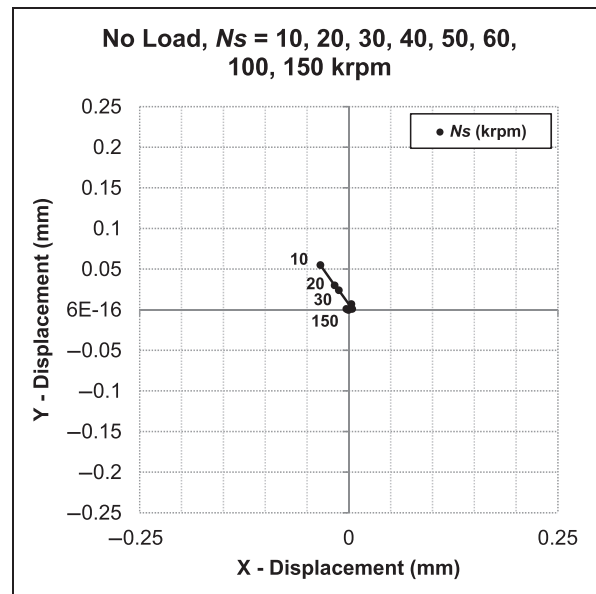


Figure 4. Predicted rotor shaft centerline at the compressor end tip (station 1) with no load at speeds 10, 20, 30, 40, 50, 60, 100, and 150 krpm.

implemented in the subject turbocharger. The radial thrust in a noncircular volute casing of the turbocharger may be approximated as

$$P = \frac{KHDB}{2.31} \quad (1)$$

where P is the radial resultant force (lb), H is the head (ft), D is the impeller diameter (in), B is the impeller overall width including shrouds (in), and K is a constant determined experimentally

$$K = 0.36 \left\{ 1 - \left(\frac{Q}{Q_n} \right)^2 \right\} \quad (2)$$

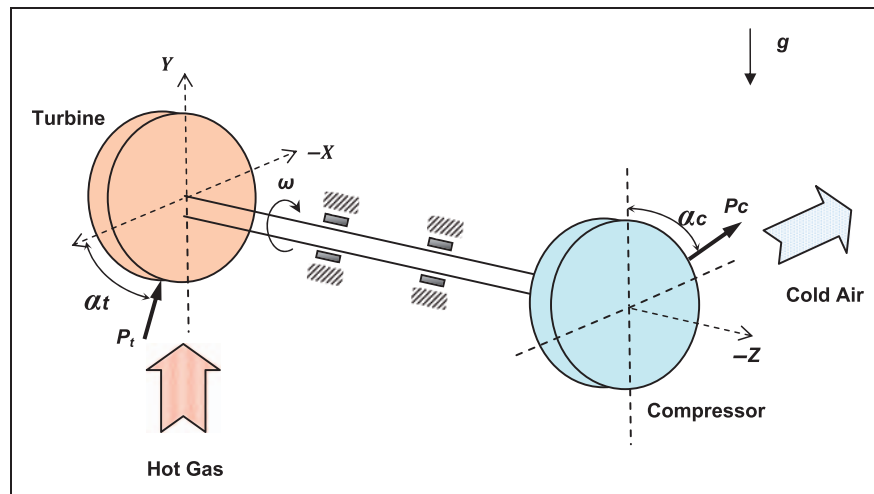


Figure 5. Radial aerodynamic loads in noncircular volute (note that the coordinate system used is similar to the analytical model but the current view is similar to the experimental test).

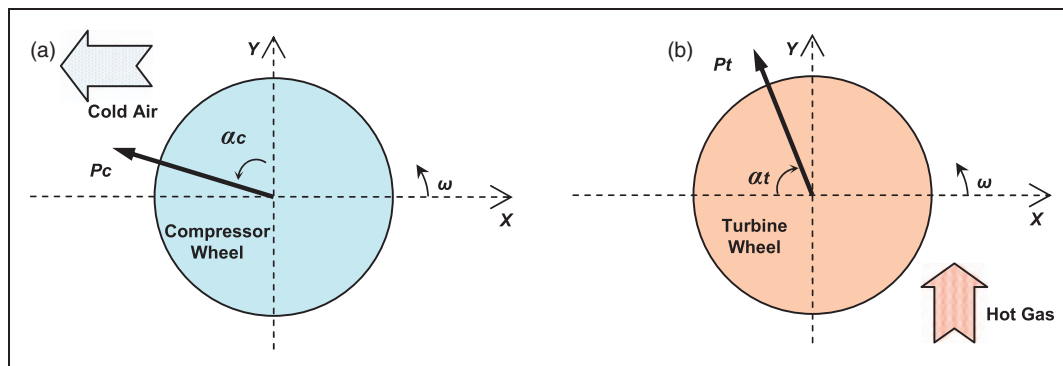


Figure 6. Radial aerodynamic force in noncircular volute on: (a) compressor wheel and (b) turbine wheel.

where Q is any capacity (gpm) and Q_n is normal capacity (gpm).

According to Stepanoff,¹⁶ the average radial aerodynamic load angle α would be 72.5° for a capacity less than normal and 265° for a capacity more than normal, as shown in Figure 5. These loads are shown in Figure 6 on the X - Y plane of the analytical model for the compressor and turbine wheels.

A computer code is developed to compute the radial thrust, P , and the thrust constant, K , in the volute casing for the turbocharger turbine and compressor for the entire estimated capacity range. The turbine diameter and width are 65 and 26.5 mm, respectively. The compressor diameter and width are 68 and 24 mm, respectively. As a starting point, the head at the turbine and compressor is assumed to be 1 and 2 ft, respectively. Knowing that the maximum air-flow of the compressor is 0.35 kg/s for the studied turbocharger, the normal capacity is assumed to be the same (0.35 kg/s = 21,000 gpm). The normal capacity of the turbine is assumed to be 10,500 gpm, which is half of the compressor capacity.

Figure 7 shows the radial thrust in a noncircular volute assumption on the compressor wheel, and

Figure 8 shows the radial thrust in a noncircular volute assumption on the turbine wheel. The thrust constant, K , is also shown in each figure with the corresponding vertical axis. Note that the thrust load is zero at normal capacity for noncircular volute assumptions. For the head values used in the analysis, the maximum absolute radial aerodynamic load is found to be less than 1 lb on the compressor wheel and less than 0.5 lb on the turbine wheel.

The next step is to numerically simulate these radial forces in the FEM in order to predict the non-linear transient response of the system. Figure 3 shows the turbocharger rotor FEM with the simulated aerodynamic forces as static forces acting on the rotor (i.e. $f_1(t) = P_c$ and $f_2(t) = P_t$). The radial compressor volute load is at station 5, and the radial turbine volute load is at station 11. Initially, the system equations of motion are numerically solved at speed 100 krpm, while varying the aerodynamic radial forces. The radial aerodynamic loads are varied at both turbocharger ends. The turbine radial load is assumed to be half of the compressor load. Two assumptions of the aerodynamic load angle, α , is considered, which

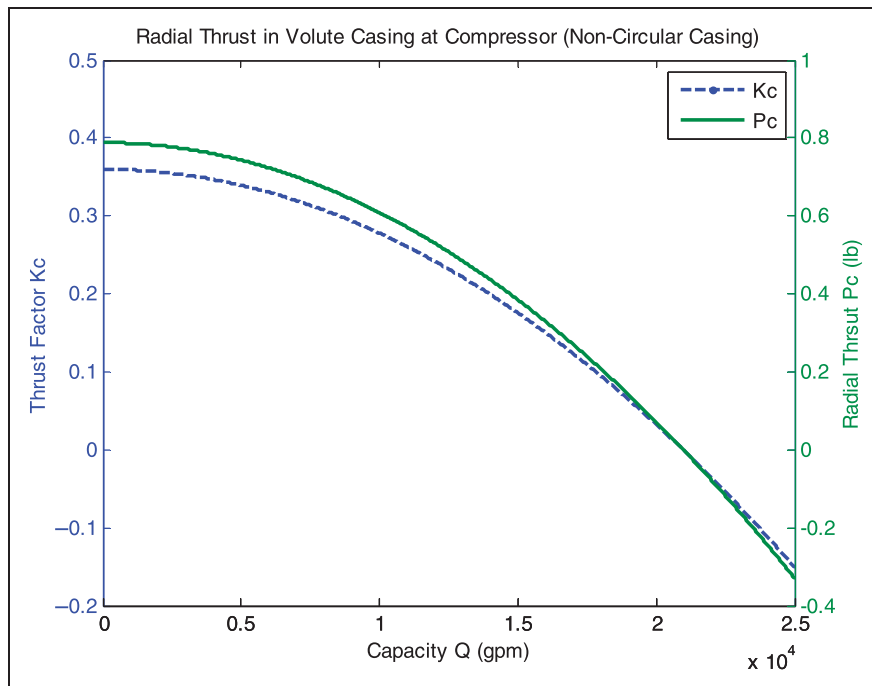


Figure 7. Computed volute radial aerodynamic forces on the compressor wheel (noncircular volute).

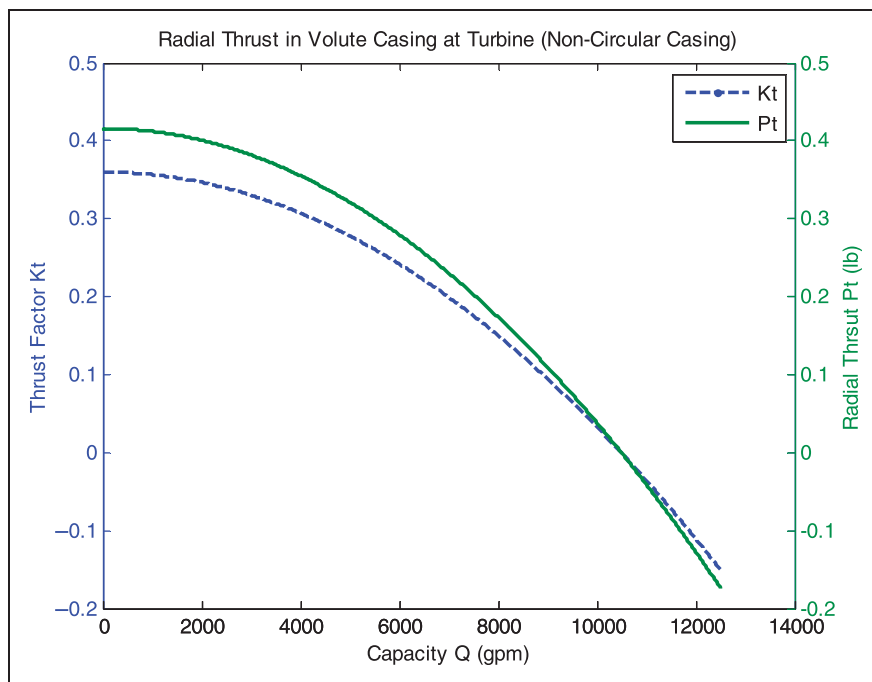


Figure 8. Computed volute radial aerodynamic forces on the turbine wheel (noncircular volute).

are 72.5° for capacity less than normal and 265° for capacity higher than normal.

Table 1 summarizes some of the computations for the steady-state orbit of the compressor end tip (station 1) at speed, N_s , 100 krpm. The steady-state compressor end shaft (station 1) centerlines for the assumption of lower than normal capacity ($\alpha = 72.5^\circ$) and higher than normal capacity ($\alpha = 265^\circ$) are plotted in Figure 9. Both the volute

radial loads are increased with the same ratio and the turbine radial loads are kept at half of the compressor radial loads. The first assumptions (Figure 9a) show that as volute radial aerodynamic loads are increased at both ends, the shaft centerline starts in the second quadrant near the X -axis and follows a relatively narrow arc as loads are increased further. At very high radial loads ($P_c = 200$ N and $P_t = 100$ N), the shaft centerline stabilizes in the third quadrant.

Table 1. Input data and predicted rotor shaft centerline at the compressor end tip (station 1) with noncircular volute radial aerodynamic forces on the compressor and turbine wheels.

Test no.	P_c (N)	P_t (N)	α_c (°)	α_t (°)	N_s (krpm)	Steady-state rotor centerline (mm)	
						X	Y
1	10	5	72.5	72.5	100	-0.021	0.00339
2	50	25	72.5	72.5	100	-0.041	0.024
3	100	50	72.5	72.5	100	-0.138	0.049
4	200	100	72.5	72.5	100	-0.175	-0.065
5	10	5	265	265	100	0.0216	0
6	50	25	265	265	100	0.031	0.014
7	100	50	265	265	100	0.156	0.089
8	200	100	265	265	100	0.199	0.084

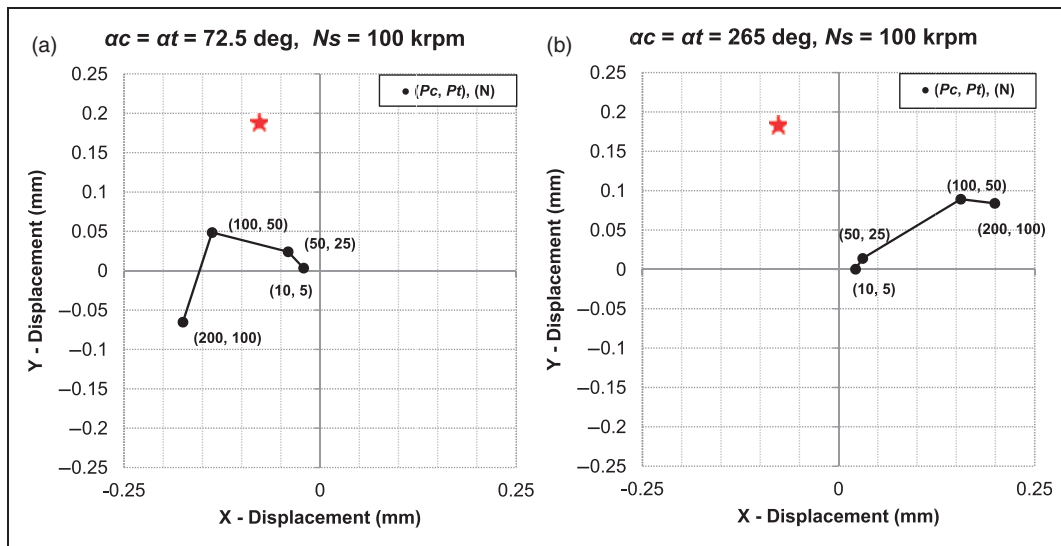


Figure 9. Predicted shaft centerline of the compressor end tip (station 1) with varied noncircular volute radial loads applied on compressor and turbine wheels at speed 100 krpm for capacity (a) lower than normal and (b) higher than normal. The star represents the experimental fully loaded shaft eccentric at about 122 krpm.

Although the centerline is in the second quadrant for the lower volute radial loads, the arc is in fact closer to the X -axis, while the experimental results of Figure 2(b) show that the shaft centerline of the loaded engine is closer to the vertical axis. On the other hand, when assuming higher capacity than normal, the trace of the shaft centerline follows a relatively wide arc that starts and ends in the first quadrant, as shown in Figure 9(b). This case is totally different in response as compared with the experimental results of the full-load test runs of Figure 2(b).

Modified noncircular volute theory

The above analysis of the radial aerodynamic forces developed in the turbocharger volute casing of either the compressor or the turbine may reveal a number of facts. The Stepanoff¹⁶ theory of centrifugal pump design is good in defining the elements that have major effects on the radial thrust but it gives

underestimated radial aerodynamic loads when applied to the turbocharger compressor volute. The experimental results of Figure 2(b) show that the average shaft eccentric is about 3 mil (0.076 mm) in the horizontal axis and 7 mil (0.178 mm) in the vertical axis, when the engine is fully loaded at high speeds. When the loaded shaft eccentric (-0.076 mm, 0.178 mm) is compared with the above-predicted results of the shaft centerline, for example Figure 9(b), then the estimate of the actual applied volute radial aerodynamic force on the compressor wheel would be above 100 N. However, the computed maximum radial aerodynamic force on the compressor wheel is about 1 N when equation (1) is used. Note that the direction of the radial load shown in Figure 9(b) does not coincide with experimental results shown in Figure 2(b).

Uchida et al.¹⁷ added to the pump design and analysis the fact that the pump characteristics and radial force are greatly affected by the size of the tongue

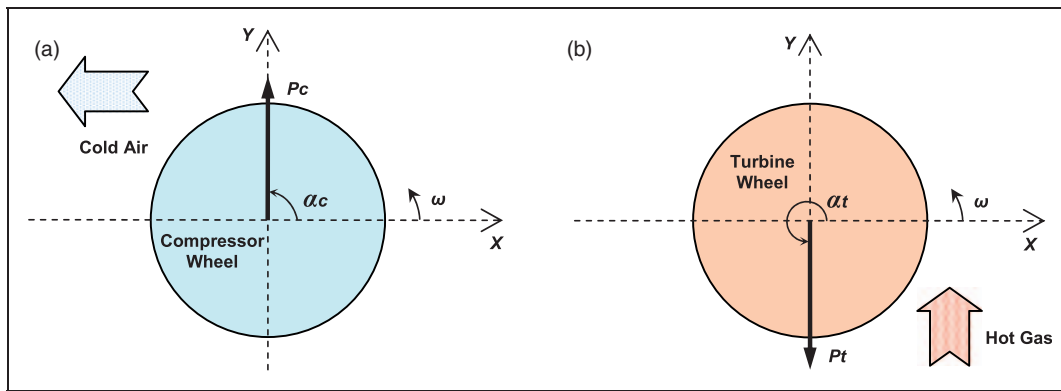


Figure 10. Predicted vertical radial aerodynamic force on the: (a) compressor wheel and (b) turbine wheel.

area, especially by the tongue shape. Radial force can be divided into two components, namely, static component and dynamic component. The dynamic component consists of the first-order component that corresponds to the shaft revolution, seventh-order component that corresponds to the number of vanes, and random component. If cavitation begins and develops, the magnitude of the radial force becomes strikingly large in the volute tongue direction.

In addition, the study by Dickmann et al.¹⁸ on the impeller blade vibration in the turbocharger centrifugal compressor showed that the position of the tongue had a significant influence on the circumferential pressure distribution at the impeller exit, despite the damping effect of the vaned diffuser. It was demonstrated that other nonaxisymmetrically positioned components, such as suction elbow, influence the circumferential pressure distribution of the rotating impeller.

The numerical predictions (Figure 9) and the experimental results (Figure 2) of the shaft centerline for turbocharger with radial aerodynamic forces indicate that the radial force could be 90° from the positive X -axis on the compressor wheel and/or 270° from the positive X -axis on the turbine wheel, as shown in Figure 10. As discussed before, there are different complicated factors that affect the value and the direction of the volute radial aerodynamic loads. Also, it seems that the radial aerodynamic force developed in the turbocharger compressor volute is the one of most concern in the literature,^{11,18} not the turbine's. Therefore, the effect of compressor volute radial aerodynamic force will be emphasized in the following analysis and the turbine radial aerodynamic force is considered to be less in magnitude, if it does exist.

The FEM predicts the steady-state orbit of the compressor end tip (station 1) at speeds, N_s , of 100 and 150 krpm when varying the compressor radial aerodynamic force with and without the turbine radial force. In the analysis, the turbine radial force, if it does exist, is assumed to be half of the compressor radial force magnitude.

The predicted shaft centerlines of the compressor end tip (station 1) with the vertical volute radial loading applied upward on the compressor wheel at speeds, N_s , of 100 and 150 krpm are plotted in Figure 11. At both speeds, as the compressor radial aerodynamic load is increased, the shaft eccentric moves vertically upward with small inclination toward the first quadrant until the radial load, P_c , becomes 50 N. As the radial load, P_c , is increased further, the shaft centerlines departs at an angle of $100\text{--}110^\circ$ from the positive X -axis, following almost a straight line, where it ends at about the point $(-0.05\text{ mm}, 0.23\text{ mm})$ for the highest applied load of 200 N. If the radial force on the compressor is 100 N, then the coordinates of the shaft eccentric is $(-0.03\text{ mm}, 0.146\text{ mm})$ at speed 100 krpm and $(-0.009\text{ mm}, 0.104\text{ mm})$ at speed 150 krpm. Knowing that the shaft eccentric of the experimental test runs at full load is about point $(-0.076\text{ mm}, 0.178\text{ mm})$, the actual compressor radial force, P_c , could be between 100 and 200 N and the actual load angle, α_c , is $100\text{--}110^\circ$.

Figure 12 shows the numerical predictions of the shaft centerline of the compressor end tip (station 1) when both the compressor and turbine radial aerodynamic loads are applied at the same time but with different magnitudes and directions at speeds 100 and 150 krpm. The turbine radial load is assumed to be 50% of the compressor radial load. However, both the compressor and turbine radial loads are increased at the same ratio. Figure 12(a) shows that as radial loads increased slightly, the shaft eccentric moves slightly upward in the first quadrant but very close to the Y -axis. As the radial loads are increased further, the shaft eccentric departs at an angle of about 110° from the positive X -axis, to reach the point $(-0.054\text{ mm}, 0.117\text{ mm})$ at compressor load, P_c , 50 N and turbine load, P_t , 25 N. When the radial load is increased further, the shaft eccentric moves upward in almost a vertical line to reach the point $(-0.05\text{ mm}, 0.234\text{ mm})$.

At speed N_s of 150 krpm, the shaft eccentric moves slightly upward in the first quadrant and remains very close to the Y -axis as the radial loads becomes 50 N

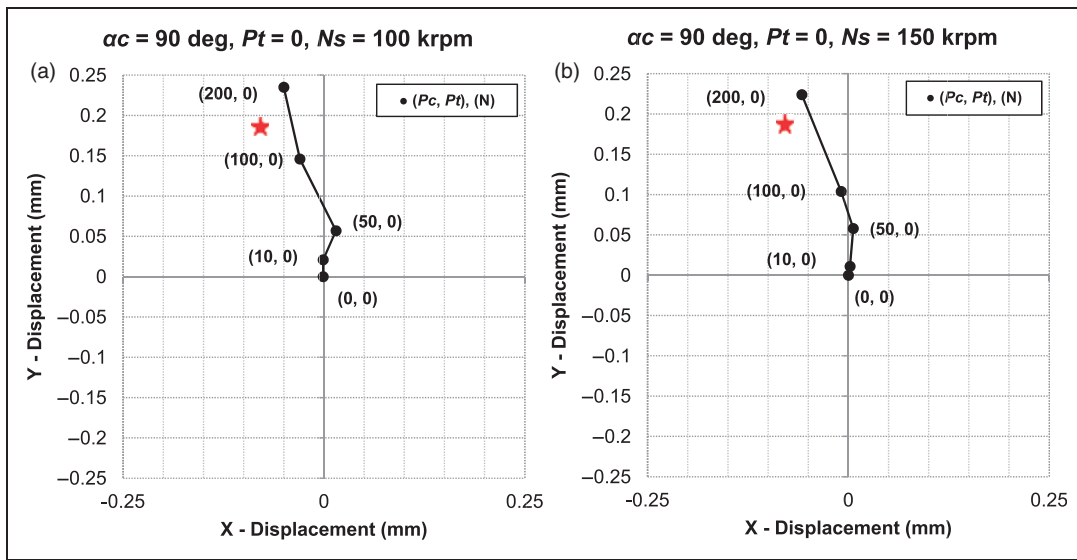


Figure 11. Predicted shaft centerline of the compressor end tip (station 1) with vertical volute radial loading applied upward on the compressor wheel at speeds (a) 100 krpm and (b) 150 krpm. The star represents the experimental fully loaded shaft eccentric at about 122 krpm.

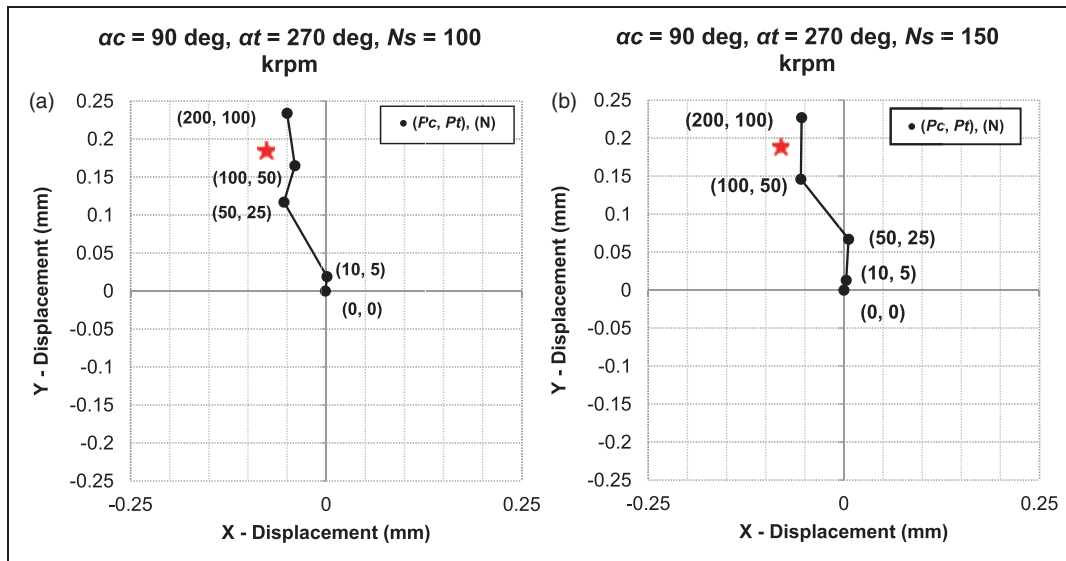


Figure 12. Predicted shaft centerline of the compressor end tip (station 1) with vertical volute radial loading applied upward on the compressor wheel and downward on the turbine wheel at speeds (a) 100 krpm and (b) 150 krpm. The star represents the experimental fully loaded shaft eccentric at about 122 krpm.

on the compressor wheel and 25 N on the turbine wheel, as shown in Figure 12(b). As the radial loads are increased further at both sides of the rotor, the shaft eccentric departs in an angle of about 130° from the positive X-axis and ends in the second quadrant at point $(-0.055 \text{ mm}, 0.146 \text{ mm})$ for the compressor radial load of 100 N and the turbine radial load of 50 N. The shaft centerline moves vertically upward as the radial loads are increased to settle in the point $(-0.054 \text{ mm}, 0.227 \text{ mm})$ for the maximum applied loads of 200 N on the compressor wheel and 100 N on the turbine wheel.

The above-mentioned numerical predictions of the turbocharger with aerodynamic radial forces on both

ends may lead to some facts. First, it is possible to have a considerable amount of radial aerodynamic force developed in the turbine volute. In addition, the angle of the compressor and turbine radial aerodynamic forces (i.e. α_c and α_t) could be about 105° and 285° , respectively.

Rotor-bearing dynamic stability

The fast Fourier transform is computed from the non-linear transient response analysis. The model predicted vibration spectrum at the compressor end tip (station 1) at speeds, N_s , of 100 and 150 krpm when varying the compressor radial aerodynamic force with

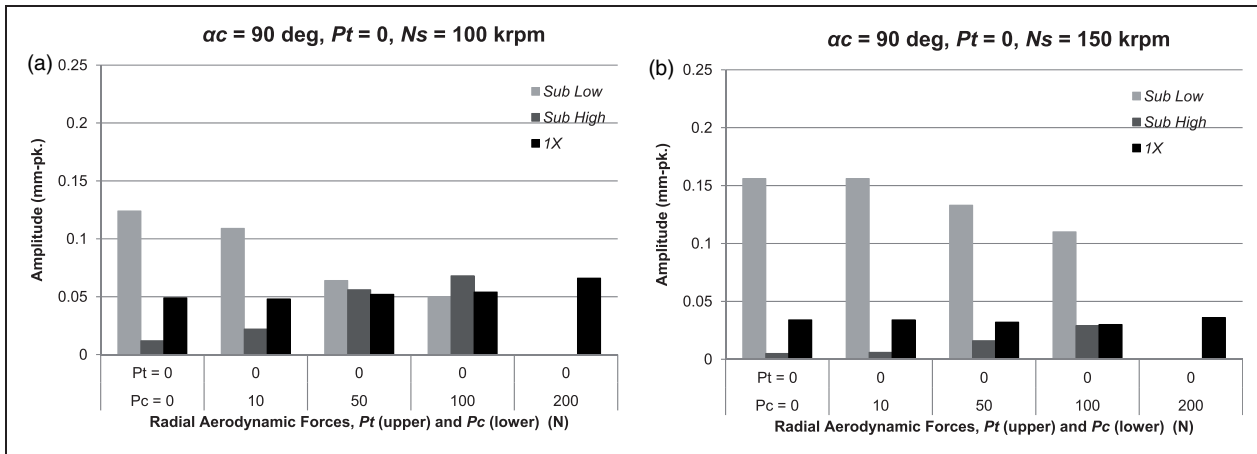


Figure 13. Predicted subsynchronous and synchronous vibrations of the compressor end tip (station 1) with vertical volute radial loading applied upward on the compressor wheel at speeds (a) 100 krpm and (b) 150 krpm.

and without the turbine radial force. In the analysis, the turbine radial force, if it does exist, is assumed to be 50% of the compressor radial force magnitude. Figure 13 represents the predicted *Sub Low* (lower frequency subsynchronous), *Sub High* (higher frequency subsynchronous), and the *1X* (synchronous) vibrations of the compressor end tip (station 1) with vertical radial aerodynamic loading, P_c , applied upward on the compressor wheel at speeds 100 and 150 krpm. At speed 100 krpm, Figure 13(a) shows that as the radial force is increased by 10 N, the *Sub Low* is decreased by 12%, the *Sub High* is increased by 45%, and the *1X* amplitude is slightly decreased. When the radial load is 50 or 100 N, both the subsynchronous and synchronous frequencies have comparable amplitudes of about 0.06 mm-pk. At the maximum applied radial load of 200 N, the rotor is totally stable with the dominant *1X* of 0.066 mm-pk and all the subsynchronous vibrations are suppressed, as shown in Figure 13(a).

At speed 150 krpm, Figure 13(b) shows that the *Sub Low* remains almost the same when the radial load is increased slowly but is reduced by 20% and 30% at radial loads 50 and 100 N, respectively. The *Sub High* amplitudes are relatively low at lower radial aerodynamic loads but reach 0.029 mm-pk at radial load of 100 N. At very high radial aerodynamic load of 200 N, the *1X* is dominant with average amplitude of 0.035 mm-pk, and both of the *Sub Low* and *Sub High* are suppressed, as shown in Figure 13(b).

From a general perspective, at speed 100 krpm, as the compressor radial aerodynamic load is increased, the *Sub Low* decreases gradually and the *Sub High* increases at the same rate to become comparable with the *Sub Low* at radial loads of 50–100 N. At the highest compressor radial aerodynamic load of 200 N, all the subsynchronous frequencies are suppressed and the *1X* is dominant at about 0.07 mm-pk. The *1X* is almost steady throughout the computations. At the highest speed of 150 krpm, the

Sub Low decreases relatively slowly as the radial load is amplified, but it is still dominant with high amplitude above 0.1 mm-pk until all the subsynchronous frequencies are suppressed at the largest radial force of 200 N, where the *1X* becomes dominant with amplitude less than 0.05 mm-pk. The *Sub High* is increased slowly as the radial load is increased but it is still below 0.05 mm-pk. The *1X* is nearly steady as the radial loads are increased.

Figure 14 shows the predicted *Sub Low* (lower frequency subsynchronous), *Sub High* (higher frequency subsynchronous), and *1X* (synchronous) vibrations of the compressor end tip (station 1), with the vertical radial aerodynamic force, P_c , applied upward on the compressor and P_t applied downward on the turbine wheel, at speeds 100 and 150 krpm. For the very low applied radial forces on the compressor and turbine (P_c, P_t), the subsynchronous and synchronous vibrations amplitudes are similar to the results of Figure 13 at the compressor load P_c of 10 N. However, Figure 14(a) shows that at the compressor load of 50 N and turbine load of 25 N, the rotor transient response exhibits a total stability with *1X* amplitude is only persist at 0.04 mm-pk. Also, at the same speed of 100 krpm and when both the radial forces are doubled ($P_c = 100$ N and $P_t = 50$ N), the unstable *Sub High* mode becomes dominant with amplitude of 0.126 mm-pk. When the radial aerodynamic load is increased further ($P_c = 200$ N and $P_t = 100$ N), the rotor response is again stable with *1X* amplitude of 0.069 mm-pk, as shown in Figure 14(a).

At speed 150 krpm, Figure 14(b) shows that the *Sub Low* remains almost the same when the radial load is increased slowly, but it is reduced by 17% at compressor radial load, P_c , of 50 N and turbine radial load, P_t , of 25 N. The *Sub High* amplitudes are relatively very low at lower radial aerodynamic loads but may reach 0.021 mm-pk when the compressor radial load is 50 N and turbine radial load is 25 N. If the radial aerodynamic loads are increased further

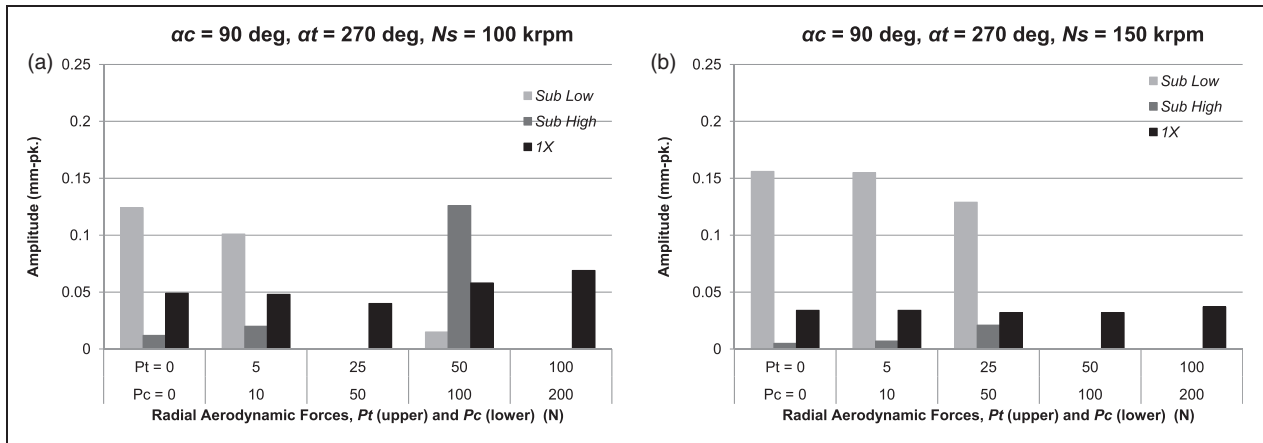


Figure 14. Predicted subsynchronous and synchronous vibrations of the compressor end tip (station 1) with vertical volute radial loading applied upward on the compressor wheel and downward on the turbine wheel at speeds (a) 100 krpm and (b) 150 krpm.

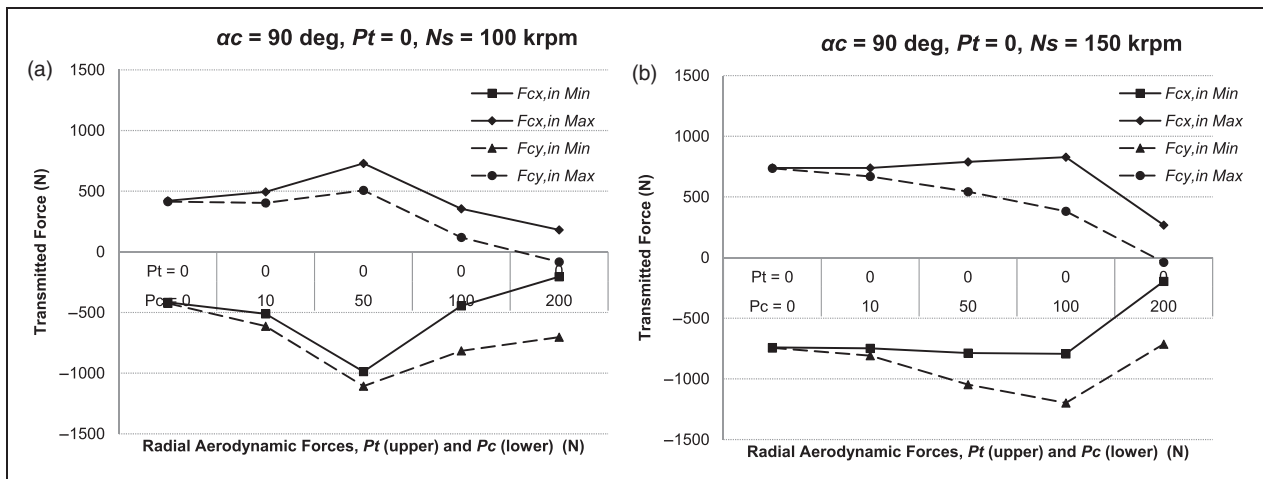


Figure 15. Predicted steady-state bearing reaction forces in the compressor bearing's inner film (station 8) with vertical radial aerodynamic forces on the compressor wheel at speeds (a) 100 krpm and (b) 150 krpm.

(i.e. $P_c = 100$ or 200 N), both the *Sub Low* and *Sub High* are suppressed and the average *1X* is 0.035 mm-pk, as can be seen in Figure 14(b).

In general, at speed 100 krpm, the subsynchronous frequencies react in the same way as predicted in Figure 13, the radial force is effective only on the compressor wheel but only for the lower applied radial forces of 10 and 5 N on the compressor and turbine wheels, respectively. When the applied radial forces are 50 and 25 N on the compressor and radial wheels, respectively, all the subsynchronous frequencies are suppressed. As the radial forces increased further, the modes of instability come up again, but the *Sub High* is dominant this time with the highest computed amplitude of 0.127 mm-pk. The response is stable with the largest applied radial forces of 200 and 100 N on the compressor and turbine wheels, respectively. At the high speed of 150 krpm, as the radial force is amplified, the *Sub Low* decreases and the *Sub High* increases, at a slow rate, until they are both suppressed for the largest applied radial forces of

200 and 100 N on the compressor and turbine wheels, respectively. The *1X* amplitudes are almost constant as the radial aerodynamic forces are increased.

Bearings reaction forces and dynamics

The steady-state bearing reaction forces are also computed in the turbocharger nonlinear analysis in order to predict the effects of the radial aerodynamic loads on those bearings. The nonlinear response of the bearing is a good estimate to the actual experimental test runs. The results of the transmitted forces in the bearings' inner and outer films demonstrate that both the films react almost equally in the single floating ring bearing. In other words, the forces transmitted to the inner film are similar to the forces transmitted to the outer film. Therefore, in the following bearing forces analysis, only the inner fluid-film forces will be considered.

Figure 15 shows the predicted steady-state bearing reaction forces in the compressor bearing's inner film

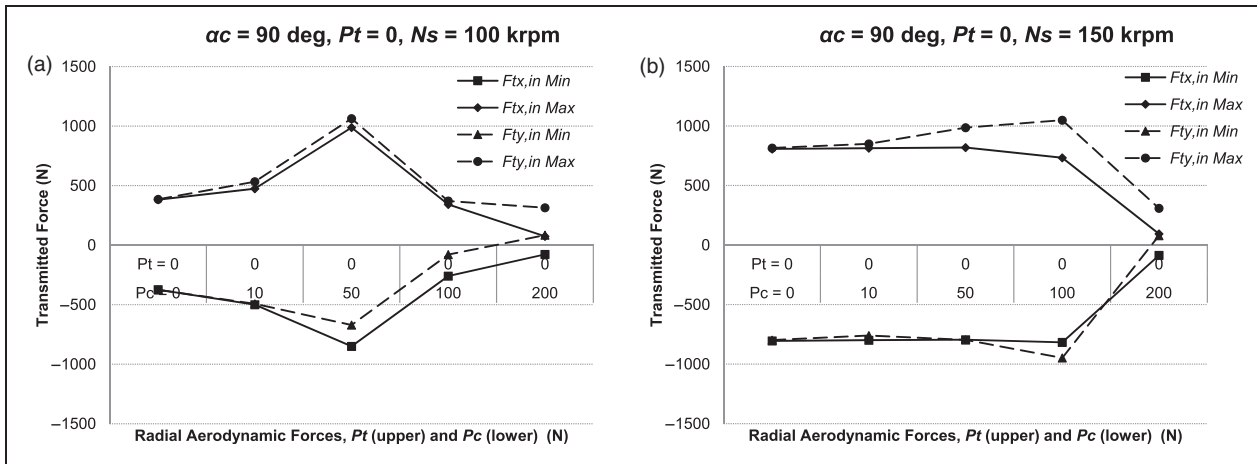


Figure 16. Predicted steady-state bearing reaction forces in the turbine bearing's inner film (station 9) with vertical radial aerodynamic forces on the compressor wheel at speeds (a) 100 krpm and (b) 150 krpm.

(station 8) with vertical volute radial aerodynamic forces on the compressor wheel ($P_t=0$) at speeds 100 and 150 krpm. At running speed of 100 krpm, when the radial aerodynamic load is increased, the absolute bearing transmitted forces are increased until the absolute peak value at compressor radial load of 50 N is reached. As the radial load is increased further, the absolute bearing transmitted forces decrease and the dominant force becomes the vertical minimum force of -703 N, as shown in Figure 15(a).

At speed 150 krpm, the compressor bearing axial reaction forces do not change much in magnitude as the radial aerodynamic load is increased, but they are reduced dramatically when the applied radial load is highest at 200 N. On the other hand, the absolute maximum vertical transmitted bearing force decreases gradually as the radial load is increased. Also, the absolute minimum vertical transmitted bearing force increases gradually as the radial load is increased, until it reaches the peak of -1198 N at radial load of 100 N; then the absolute value decreases at radial load of 200 N but it becomes the dominant bearing force with -713 N.

Figure 16 shows the predicted steady-state bearing reaction forces in the turbine bearing's inner film (station 9) with vertical volute radial aerodynamic forces on the compressor wheel ($P_t=0$) at speeds 100 and 150 krpm. At running speed of 100 krpm, when the radial aerodynamic load is increased, the absolute bearing transmitted forces are increased until the absolute peak value at compressor radial load of 50 N is reached, as shown in Figure 16(a). As the radial load is increased further, the absolute bearing transmitted forces decrease, and the dominant force becomes the vertical maximum force of 314 N.

Similar to the compressor bearing, at speed 150 krpm, the turbine bearing axial reaction forces do not change much in magnitude as the radial aerodynamic load is increased, but they are reduced dramatically when the applied radial load is highest (i.e. 200 N). The maximum vertical transmitted bearing

force increases slowly as the radial load is increased, but it decreases significantly at highest radial load of 200 N. Also, as the radial load is increased, the absolute minimum vertical transmitted bearing force remains almost at the same value; it increases by about 20% at radial load of 100 N, after that it decreases sharply at the highest applied load of 200 N.

In general, at speed 100 krpm, the transmitted peak–peak forces in the compressor and turbine bearings are comparable at compressor radial aerodynamic load of 50 N, with an average transmitted bearing force of about 1650 N pk-pk, as shown in Figures 15(a) and 16(a). These peak–peak transmitted forces decrease as the compressor radial force is further increased, but their values are almost double at the compressor bearing.

In addition, at speed 150 krpm, the peak–peak axial bearing forces of the turbine end and the compressor ends are comparable and almost steady as the compressor radial aerodynamic force is increased until they decrease significantly at the largest applied radial load of 200 N, as shown in Figures 15(b) and 16(b). The peak–peak vertical bearing force is highest at the turbine bearing with 1997 N pk-pk at radial load of 100 N. The minimum peak vertical bearing force is lowest at the compressor bearing with -1198 N-pk at the radial load of 100 N. When the applied radial aerodynamic load is largest at 200 N, the maximum peak–peak and maximum peak bearing forces are in the compressor bearing.

Figure 17 shows the predicted steady-state bearing reaction forces in the compressor bearing's inner film (station 8) with the vertical radial aerodynamic forces applied on both the compressor and turbine wheels at speeds 100 and 150 krpm. Figure 17(a) shows that the average bearing forces increase slowly as the radial loads are increased, but then they decrease to reach minimum values when the radial loads on the compressor and the turbine are 50 and 25 N, respectively. That might be due to the fact that all the unstable modes are suppressed, as was shown in Figure 14(a).

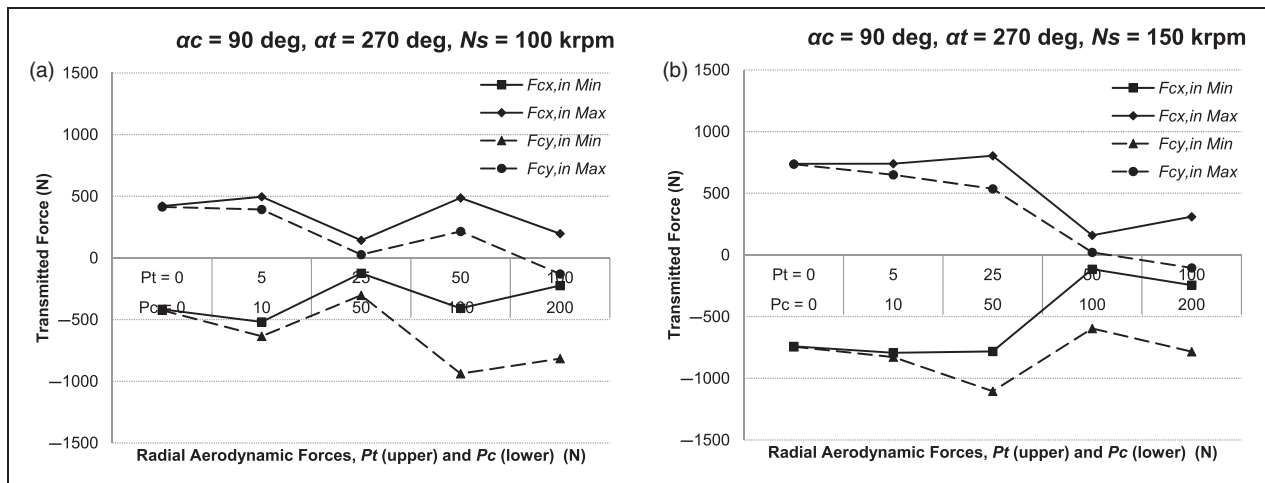


Figure 17. Predicted steady-state bearing reaction forces in the compressor bearing's inner film (station 8) with vertical radial aerodynamic forces on the compressor and turbine wheels at speeds (a) 100 krpm and (b) 150 krpm.

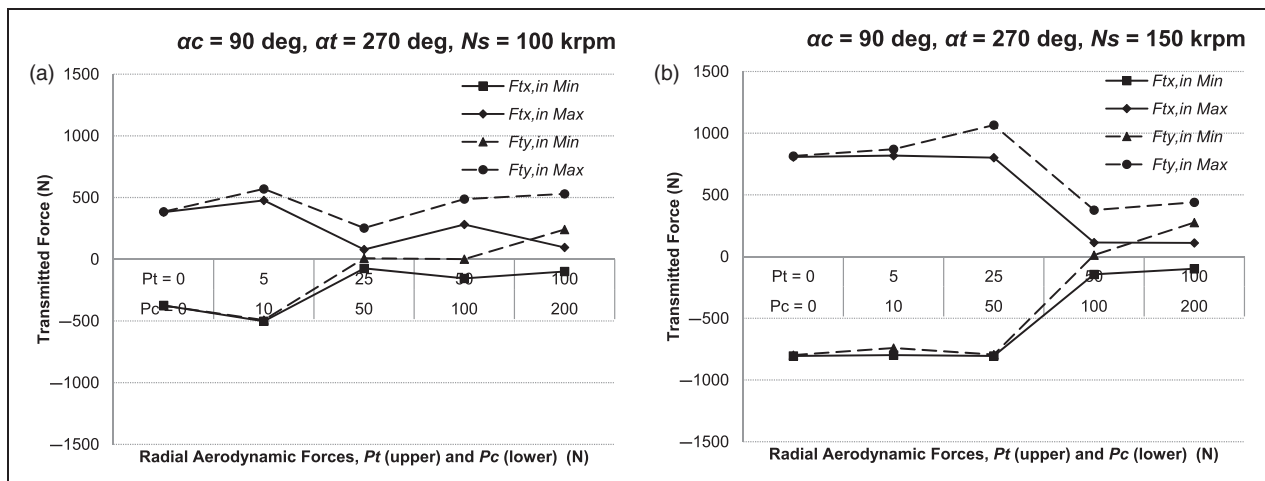


Figure 18. Predicted steady-state bearing reaction forces in the turbine bearing's inner film (station 9) with vertical radial aerodynamic forces on the compressor and turbine wheels at speeds (a) 100 krpm and (b) 150 krpm.

The transmitted bearing forces increase again as the radial loads are increased to reach the maximum absolute vertical force of -938 N at radial loads of 100 N on the compressor wheel and 50 N on the turbine wheel. That could be due the rebuilding of the modes of instability, as was shown in Figure 14(a). The bearing forces decrease again as the radial loads are increased, and the vertical force remains dominant with -816 N at highest applied radial loads (i.e. $P_c = 200$ N and $P_t = 100$ N).

The axial compressor-bearing forces remains relatively steady at speed 150 krpm, as the radial loads are increased, which can be seen in Figure 17(b). However, when the compressor radial load is 100 N and the turbine radial load is 50 N, the axial compressor-bearing forces decrease dramatically and then slowly increase at radial loads of 200 and 100 N on the compressor and turbine wheels, respectively. In addition, as the radial loads are increased, the absolute value of the maximum vertical compressor-bearing force decreases

but the absolute value of the minimum vertical bearing force increases, until the radial aerodynamic forces becomes 50 N on the compressor and 25 N on the turbine. After that, the absolute value of the vertical compressor-bearing forces decreases at radial loads of 100 N on the compressor and 50 N on the turbine; then both the bearing forces increase slowly at the highest radial forces, where the minimum vertical bearing force becomes the largest with -784 N, as displayed in Figure 17(b).

Figure 18 represents the predicted steady-state bearing reaction forces in the turbine bearing's inner film (station 9) with vertical radial aerodynamic forces applied on the compressor and turbine wheels, at speeds 100 and 150 krpm. At speed 100 krpm, Figure 18(a) shows that the turbine-bearing forces increase as the radial aerodynamic forces are increased, but then the bearing forces decrease to reach the minimum absolute values at radial forces of 50 N on the compressor and 25 N on the turbine.

These turbine-bearing reaction forces seem to be similar to the compressor-bearing's forces at the aforementioned radial aerodynamic forces (i.e. $P_c = 10\text{--}50\text{ N}$ and $P_t = 5\text{--}25\text{ N}$). As the radial forces are increased further, the absolute minimum and maximum turbine-bearing forces increase and then become almost steady with the highest radial forces.

At speed 150 krpm, the turbine-bearing transmitted forces are almost steady until the radial aerodynamic forces become 50 N on the compressor and 25 N on the turbine, with exception being the maximum vertical bearing forces, where it increases by 30%, as shown in Figure 18(b). All the turbine-bearing reaction forces decrease dramatically when the radial aerodynamic forces are 100 N on the compressor wheel and 50 N on the turbine wheel. Most of the bearing forces become relatively steady at higher radial aerodynamic loads, but the minimum vertical bearing force increases and reduces the gap between the minimum and maximum vertical bearing forces, as can be seen in Figure 18(b).

In addition, at speed 100 krpm, the transmitted peak–peak forces in the compressor and turbine bearings are comparable at the lower applied radial aerodynamic loads ($P_c \leq 50\text{ N}$ and $P_t \leq 25\text{ N}$), as can be seen in Figures 17(a) and 18(a). Although the transmitted bearing forces are fluctuating in both bearings as the radial loads are further increased, the decrease of peak–peak transmitted forces is relatively larger at the compressor bearing.

Similar to the turbocharger with applied aerodynamic loads on the compressor only, at speed 150 krpm, the peak–peak axial bearing forces of the turbine end and the compressor ends are comparable and almost steady as the compressor radial aerodynamic force is increased until they decrease significantly at the compressor and turbine radial loads of 100 and 50 N, respectively, as shown in Figures 17(b) and 18(b). The peak–peak vertical bearing force is highest at the turbine bearing with 1860 N pk-pk at radial loads of 50 and 25 N on the compressor and turbine wheels, respectively. The minimum peak vertical bearing force is lowest at the compressor bearing with -1105 N-pk at radial loads of 50 and 25 N on the compressor and turbine wheels, respectively. When the applied radial aerodynamic load is largest at 200 and 100 N on the compressor and turbine wheels, respectively, the maximum peak–peak and maximum peak bearing forces are in the compressor bearing, as shown in Figures 18(b) and 17(b).

Figure 19 shows the numerically predicted steady-state rotor shaft X – Y orbit at the bearings stations (stations 8 and 9) at speed 100 krpm, with the simulated compressor radial aerodynamic loads of 50 and 200 N, respectively. One may observe the chaotic response of the rotor shaft in the compressor bearing (see Figure 19a) when the applied radial load is 50 N on the compressor wheel and the transmitted forces in the compressor bearing are highest (see Figure 15a). It is important to mention that rubbing was not

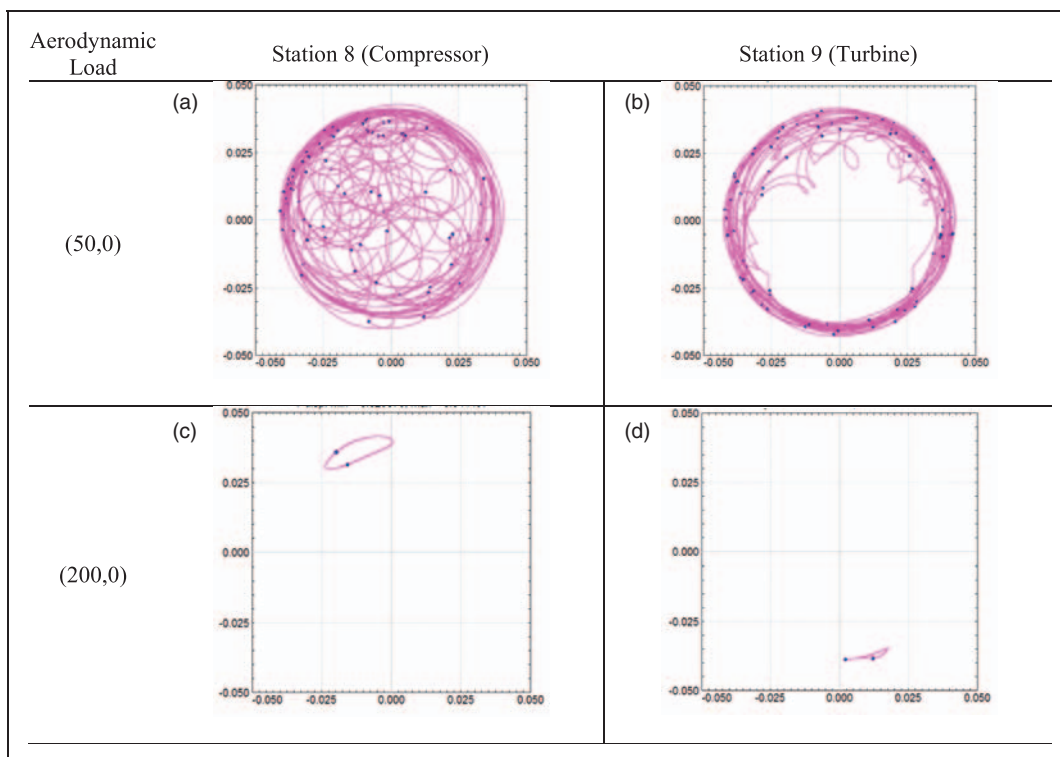


Figure 19. Predicted steady-state X – Y rotor response in compressor bearing (station 8) and turbine bearing (station 9) with vertical radial aerodynamic force on the compressor wheel at speed 100 krpm.

observed in the bearings or the impeller tips even for excursions as high as 750 μm at the target nut. Moreover, the X - Y orbits in Figure 19(c) show stable steady-state response at both bearings but with relatively large offset from the bearing center and that may predict the absence of the modes of instability, which was also predicted in Figure 13(a) for the most aerodynamically loaded rotor.

Figure 20 shows the numerically predicted steady-state rotor shaft X - Y orbit at the bearings stations

(stations 8 and 9) at speed 100 krpm, with simulated compressor radial aerodynamic loads of 10, 50, 100, and 200 N, respectively, while the turbine radial loads are always half of that of the compressor. As shown in Figure 20(a) and (b), the rotor shaft whirls in both bearings with a high limit cycle as the *Sub Low* is dominant. At applied radial aerodynamic loads of 50 and 25 N, on the compressor and turbine wheels, respectively, the rotor whirls in a stable small and narrow orbit, as shown in Figure 20(c) and (d).

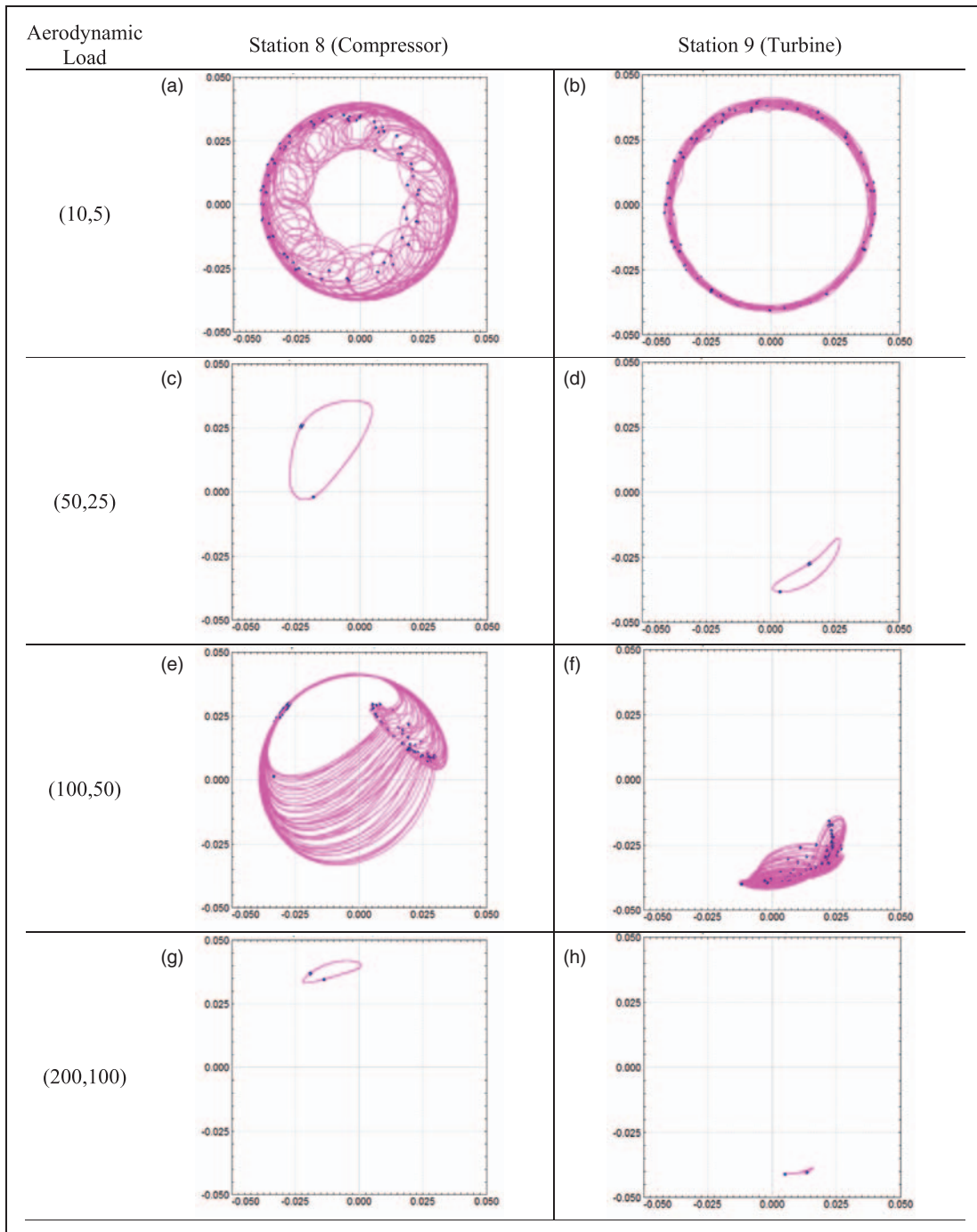


Figure 20. Predicted steady-state X - Y rotor response in compressor bearing (station 8) and turbine bearing (station 9) with vertical radial aerodynamic forces on both of the compressor and the turbine wheels at speed 100 krpm.

As there are two timing marks, this may indicate the presence of the second synchronous ($2X$) frequency but probably at relatively much lower amplitude than $1X$. Figure 20(e) and (f) show the whirling of the rotor in bearings when the *Sub High* is the dominant frequency, as was predicted in Figure 14. At the highest applied radial loads, the rotor is stable with the shaft centerline away from the center, as shown in Figure 20(g) and (h).

Conclusions

This study investigated the radial aerodynamic forces that may develop inside the compressor and the turbine volutes and their effects on the dynamics and the stability of the rotor-bearing system. The numerical predictions were correlated with the experimental results in the VT Rotor Dynamic Lab¹⁰ that observed a side load force when the engine is loaded at full speed, which moves the shaft eccentric. A modified noncircular volute theory is used to describe the aerodynamic loading profile and showed good agreement with experimental results. The turbocharger FEM was developed with the simulated radial aerodynamic forces as static forces on the compressor and the turbine stations in order to solve for the nonlinear time-transient response. The results of the current study are can be summarized as follows:

1. When the radial aerodynamic force is applied only on the compressor wheel (Figure 13), as the compressor radial aerodynamic load is increased, the *Sub Low* decreases gradually. The *Sub High* increases, at speed 100 krpm, at the same rate to become comparable with the *Sub Low* at radial loads of 50–100 N, while it is increased slowly, at speed 150 krpm. At the highest compressor radial aerodynamic load of 200 N, all the subsynchronous frequencies are suppressed and the $1X$ is dominant.
2. When the radial aerodynamic forces are applied on both the compressor and turbine wheels (Figure 14), at speed 100 krpm, the subsynchronous frequencies decrease for the lower applied radial forces on the compressor and turbine wheels until all the subsynchronous frequencies are suppressed. As the radial forces increased further, the modes of instability come up again, but the *Sub High* is dominant this time. The response is stable with the largest applied radial forces of 200 and 100 N on the compressor and turbine wheels, respectively. At the high speed of 150 krpm, as the radial force is amplified, the *Sub Low* decreases and the *Sub High* increases, at a slow rate, until they are both suppressed for the largest applied radial forces. The $1X$ amplitudes are almost constant as the radial aerodynamic forces are increased.
3. When the radial aerodynamic force is only applied on the compressor wheel, at speed 100 krpm, the transmitted peak–peak forces in the compressor

and turbine bearings are comparable at compressor radial aerodynamic load of 50 N (Figures 15 and 16). These peak–peak transmitted forces decrease as the compressor radial force is further increased, but their values are almost double at the compressor bearing. At speed 150 krpm, the peak–peak axial bearing forces of the turbine end and the compressor ends are comparable and almost steady as the compressor radial aerodynamic force is increased until they decrease significantly at the largest applied radial load of 200 N. When the applied radial aerodynamic load is largest at 200 N, the maximum peak–peak and maximum peak bearing forces are in the compressor bearing.

4. When the radial aerodynamic forces are applied on both the compressor and turbine wheels, at speed 100 krpm, the transmitted peak–peak forces in the compressor and turbine bearings are comparable at the lower applied radial aerodynamic loads. Although the transmitted bearing forces are fluctuating in both bearings as the radial loads are further increased, the decrease in the peak–peak transmitted forces is relatively larger at the compressor bearing. At speed 150 krpm, the change in the reaction forces is similar to the turbocharger with applied aerodynamic loads on the compressor only, when the applied radial aerodynamic loads are largest at 200 and 100 N on the compressor and turbine wheels, respectively, the maximum peak–peak and maximum peak bearing forces are in the compressor bearing.

In general, the numerical predictions demonstrated that as the radial aerodynamic forces were increased, the *Sub Low* amplitudes were reduced and the *Sub High* amplitudes were increased, until all the instabilities are totally suppressed when the radial forces were overloaded. The results demonstrated that radial aerodynamic forces have direct influence on the dynamic stability and on the bearing reaction forces, and those aerodynamic forces should be considered in any linear and nonlinear analyses of the bearings and the rotor-bearing system. The assumption of static aerodynamic forces provides a qualitative insight into the dynamic stability and bearing reaction forces. Therefore, including the dynamic component of the aerodynamic force is crucial to the development of optimum turbocharger design. In this regard, the use of CFD would provide an accurate estimation for the pressure distribution inside the volute aerodynamic forces. Moreover, future work includes studying the influence of the radial aerodynamic forces on the bearings dynamic coefficients and investigating how those forces affect the linearized stiffness and damping coefficients.

Funding

The authors acknowledge the financial support provided by the King Fahd University of Petroleum and Minerals and

King Abdullah University of Science and Technology to conduct this research.

References

1. Watson N and Janota MS. *Turbocharging the internal combustion engine*. London, UK: Macmillan Press, 1982.
2. Holmes R, Brennan MJB and Gottrand B. Vibration of an automotive turbocharger: a case study. In: *Vibrations in rotating machinery, 8th international conference on vibrations in rotating machinery*, Swansea, UK, 7–9 September 2004, pp. 445–455. New York, NY: Wiley.
3. San Andres L and Kerth J. Thermal effects on the performance of floating ring bearings for turbochargers. *Proc IMechE, Part J: J Engineering Tribology* 2004; 218(5): 437–450.
4. Flaxington D and Swain E. Turbocharger aerodynamic design. *Proc IMechE, Part C: J Mechanical Engineering Science* 1999; 213(1): 43–57.
5. Yao J, Yao YF, Manson PJ, et al. Computational prediction of local distorted flow in turbocharger. In: PFG Zhuang and PJC Li (eds) *New trends in fluid mechanics research*. Berlin: Springer, 2009, pp.154–157.
6. Chen H. Recent challenges in the aerodynamic development of turbocharger compressors for gasoline passenger cars. In: *9th international conference on turbochargers and turbocharging*, London, UK, 19–20 May 2010, pp. 125–133. Cambridge, UK: Woodhead Publishing Ltd.
7. Romagnoli A. *Aerodynamic and thermal characterization of turbocharger turbines: experimental and computational evaluation*. PhD Thesis, Imperial College London, UK, 2010.
8. Romagnoli A and Martinez-Botas R. Performance prediction of a nozzleed and nozzleless mixed-flow turbine in steady conditions. *Int J Mech Sci* 2011; 53(8): 557–574.
9. Rajoo S, Romagnoli A and Martinez-Botas RF. Unsteady performance analysis of a twin-entry variable geometry turbocharger turbine. *Energy* 2010; 38(1): 176–189.
10. Kirk RG, Kornhauser AA, Sterling J, et al. Turbocharger on-engine experimental vibration testing. *J Vib Control* 2010; 16(3): 343–355.
11. Eynon PA and Whitfield A. Pressure recovery in a turbocharger compressor volute. *Proc IMechE, Part A: J Power and Energy* 2000; 214(6): 599–610.
12. Chen WJ and Gunter EJ. *Introduction to dynamics of rotor-bearing systems*. Victoria, BC, Canada: Trafford Publishing, 2005.
13. Alsaeed AA. *Dynamic stability evaluation of an automotive turbocharger rotor-bearing system*. MS Thesis, Virginia Polytechnic Institute and State University, Blacksburg, VA, USA, 2005.
14. Kirk RG, Alsaeed AA and Gunter EJ. Stability analysis of a high-speed automotive turbocharger. *Tribol Trans* 2007; 50(3): 427–434.
15. Gordon Kirk R and Alsaeed AA. Induced unbalance as a method for improving the dynamic stability of high-speed turbochargers. *Int J Rotating Mach* 2011; 2011: ■■–■■.
16. Stepanoff AJ. *Centrifugal and axial flow pumps: theory, design, and application*. New York, NY: Wiley, 1957.
17. Uchida N, Imaichi K and Shirai T. Radial force on the impeller of a centrifugal pump. *Bull JSME* 1971; 14(76): 1106–1117.
18. Dickmann H-P, Secall Wimmel T, Szwedowicz J, et al. Unsteady flow in a turbocharger centrifugal compressor: three-dimensional computational fluid dynamics simulation and numerical and experimental analysis of impeller blade vibration. *J Turbomach* 2006; 128(3): 455–465.